

A novel numerical scheme for nonlinear electron-plasma oscillations

Prabal Singh Verma

CNRS, Aix-Marseille Univ., PIIM, UMR 7345, Marseille F-13397, France

(Dated: November 9, 2018)

In this work, we suggest an easy-to-code higher-order finite volume semi-discrete scheme to analyze the nonlinear behavior of the electron-plasma oscillations by solving electron fluid equations numerically. The present method employs a fourth-order accurate centrally weighted essentially nonoscillatory reconstruction (CWENO4) polynomial for estimating the numerical flux at the grid-cell interfaces, and a fourth-order Runge-Kutta method for the time integration. The numerical implementation is validated by reproducing earlier results for both non-dissipative and dissipative cold plasmas. The stability of the present scheme is illustrated by evolving the nonlinear electron plasma oscillations in a cold non-dissipative plasma for hundred plasma periods, which also display a negligible numerical dissipation. The fourth-order accuracy of the existing approach is also confirmed by evaluating the convergence of errors for the nonlinear electron plasma oscillations in a cold non-dissipative plasma.

I. INTRODUCTION

Numerical simulations have always been very useful to illustrate the physics of a strongly nonlinear system for which an analytical approach is not feasible [1–6]. The primary focus of this manuscript is to introduce a new numerical scheme for studying nonlinear electrostatic plasma oscillations in various physical regimes. Investigation of nonlinear electrostatic oscillations in different plasmas is a fascinating field of research for more than five decades [7–20]. One of the leading application of these studies is in the laser or particle beam induced wake-field acceleration experiments and simulations, where one aims at attaining mono-energetic charged particles in short distances, e.g. [21, 22]. Depending upon the problem of interest multiple numerical methods, for example, the Particle-In-Cell (PIC) simulation [23], the Vlasov simulation, e.g. [24, 25], the sheet simulation [3, 13] and the direct numerical simulations of the fluid equations, e.g. [1, 2, 26, 27] are being practiced widely in the literature. In the PIC simulation, charged particles are evolved in time by solving the coupled Lorentz force equation and Maxwell’s equations. In the Vlasov simulation, the distribution function of a system, combined with the Poisson’s equation, is developed in time. The sheet simulation deals with the evolution of the physical quantities in Lagrange coordinates and is quite similar to the fluid simulation in the sense that it leads to unphysical results after the sheet-crossing (wave-breaking) [7].

Wave-breaking is a nonlinear physical process that translates the coherent energy into random kinetic energy as a result of the wave-particle interactions. It occurs when the nearby sheets or the fluid elements, taking part in the coherent oscillations, cross each other. One of the advantages of the PIC and the Vlasov simulations over fluid simulations is that the formers are capable of illustrating the physics of the wave-particle interactions, and therefore these numerical tools can be used to study the dynamics of the plasma species even beyond the wave-breaking [4, 5]. Nevertheless, these simulations are computationally very expensive and exhibit

a significant noise, especially in spatial profiles of the charge density fluctuations. On the contrary, sheet simulations show negligible noise (numerical error), and it is also probable to make them deliver physical results even beyond the sheet crossing (wave-breaking). However, the main limitation of these simulations is that they cannot be stretched to study the dynamics of a multi-component plasma. Therefore, we here propose a simple numerical scheme to solve the electron fluid equations, which delivers comparatively more accurate result when the wave-particle interactions are not essential and can easily be extended to multi-species plasma.

Note here that usually a finite difference scheme based on flux corrected transport [28] is utilized to study nonlinear electrostatic oscillations in different physical regimes, e.g. [2, 26, 27]. As an alternative, we here present an easy-to-implement higher-order finite volume semi-discrete scheme, based on a fourth-order centrally weighted essentially nonoscillatory (CWENO4) reconstruction [29] and a fourth order Runge-Kutta method, for the same. The CWENO approach, which is originally based on WENO approach (see, for example, [30]), is being used widely to solve multi-dimensional hyperbolic problems [29, 31–37]. We are, however, employing this classical approach, for the first time, to analyze nonlinear electrostatic oscillations in a cold electron-ion plasma, where the ions are considered to be infinitely massive. In order to validate the implementation, we first rediscover the earlier results for both non-dissipative and dissipative cold plasmas. Later we test the stability and the numerical dissipation of the numerical scheme by following the evolution of the nonlinear electron plasma oscillations up to hundred of plasma periods. We do not observe any visible dissipation and unphysical effect (e.g. numerical noise) in this test. We then confirm the fourth-order accuracy of the present numerical scheme by estimating the error convergence for nonlinear electron plasma oscillations.

The flow of the present manuscript is as follows. In section II, we introduce the electron fluid equations and rewrite them in the conservative form. In section III, a

semidiscrete scheme is introduced to solve electron fluid equation numerically. Section IV deals with the validation and accuracy of the numerical implementation. In section V we provide the summary of the present work and discussion.

II. GOVERNING EQUATIONS

The basic equations governing the dynamics of the electron fluid in a cold homogeneous, unmagnetized, dissipative plasma, are the momentum equation, the continuity equation, Poisson's equation and the current equation:

$$\frac{\partial v_e}{\partial t} + v_e \frac{\partial v_e}{\partial x} = -E + \frac{1}{n_e} \frac{\partial}{\partial x} \left(\nu_e \frac{\partial v_e}{\partial x} \right) - \eta v_e, \quad (1)$$

$$\frac{\partial n_e}{\partial t} + \frac{\partial(n_e v_e)}{\partial x} = 0, \quad (2)$$

$$\frac{\partial E}{\partial x} = 1 - n_e, \quad (3)$$

$$\frac{\partial E}{\partial t} = v_e n_e. \quad (4)$$

Here we assume that the spatial variations are only along the x -direction, therefore derivatives along the other directions (y, z) are not present in the above equations. Moreover, for simplicity ions are considered to be static and homogeneously distributed in space. Note that the Eqs.(1)-(4) are in normalized form, where $x \rightarrow k^{-1}$, $t \rightarrow \omega_{pe}^{-1}$, $n_e \rightarrow n_0$, $E \rightarrow \frac{m\omega_{pe}^2}{ke}$, $v_e \rightarrow \frac{\omega_{pe}}{k}$, $\nu_e \rightarrow \frac{mn_0\omega_{pe}}{k^2}$, $\eta \rightarrow \frac{m\omega_{pe}}{n_0e^2}$. Here ν_e is the electron viscosity, η is the plasma resistivity and rest of the symbols have their usual definitions. Since for realistic situations $\nu_e(x, t)$ can be considered to be constant, we assume $\nu_e = \nu_0$ which now can be taken out of the partial derivative in Eq.(1) [2]. Thus, Eqs.(1)-(4) can also be expressed as,

$$n_e \frac{\partial v_e}{\partial t} + n_e v_e \frac{\partial v_e}{\partial x} = -n_e E + \nu_0 \frac{\partial^2 v_e}{\partial x^2} - \eta n_e v_e, \quad (5)$$

$$\frac{\partial n_e}{\partial t} + \frac{\partial(n_e v_e)}{\partial x} = 0, \quad (6)$$

$$\frac{\partial E}{\partial t} + v_e \frac{\partial E}{\partial x} = v_e. \quad (7)$$

Equations (5)-(7) can be further written in the conservative form as follows,

$$\frac{\partial(n_e v_e)}{\partial t} + \frac{\partial(n_e v_e^2)}{\partial x} = -n_e E + \nu_0 \frac{\partial^2 v_e}{\partial x^2} - \eta n_e v_e, \quad (8)$$

$$\frac{\partial n_e}{\partial t} + \frac{\partial(n_e v_e)}{\partial x} = 0, \quad (9)$$

$$\frac{\partial n_e E}{\partial t} + \frac{\partial(n_e E v_e)}{\partial x} = n_e v_e. \quad (10)$$

The above-mentioned equations can be written in a more compact form:

$$\frac{\partial \mathbf{U}}{\partial t} + \frac{\partial \mathbf{F}}{\partial x} = \mathbf{S}, \quad (11)$$

where $\mathbf{U} = (n_e v_e, n_e, n_e E)$ is the vector of conserved quantities, $\mathbf{F} = (n_e v_e^2, n_e v_e, n_e E v_e)$ is the corresponding vector of fluxes along the x -direction, and $\mathbf{S} = (-n_e E + \nu_0 \frac{\partial^2 v_e}{\partial x^2} - \eta n_e v_e, 0, n_e v_e)$ is the vector of the respective source terms.

In Sec.III we will discuss the finite volume method to solve Eq.(11) numerically.

III. NUMERICAL SCHEME

In order to solve Eq.(11) numerically we discretize the computational domain $[0, l_x]$ into small grid cells where l_x is the length of the domain along the x -direction. Suppose n_x is the number of grid cells along the x -direction then the grid-cell size becomes $\Delta x = l_x/n_x$. Now consider a grid cell i centered at x_i and perform the line integration of Eq.(11) about the grid cell as,

$$\frac{1}{\Delta x} \int_{x_{i-1/2}}^{x_{i+1/2}} dx \left[\frac{\partial \mathbf{U}}{\partial t} + \frac{\partial \mathbf{F}}{\partial x} = \mathbf{S} \right], \quad (12)$$

here $x_{i\pm 1/2} = x_i \pm \Delta x/2$ correspond to the positions of grid cell interfaces along the x -direction. Eq.(12) can be further rewritten as,

$$\frac{d\bar{\mathbf{U}}_i}{dt} = -\frac{\mathbf{F}_{i+1/2} - \mathbf{F}_{i-1/2}}{\Delta x} - \bar{\mathbf{S}}_i. \quad (13)$$

Here $\bar{\mathbf{U}}_i, \bar{\mathbf{S}}_i$ are the averages of \mathbf{U}, \mathbf{S} , respectively in the grid cell i and are defined as,

$$\bar{\mathbf{U}}_i(t) = \frac{1}{\Delta x} \int_{x_{i-1/2}}^{x_{i+1/2}} dx \mathbf{U}(x, t), \quad (14)$$

$$\bar{\mathbf{S}}_i(t) = \frac{1}{\Delta x} \int_{x_{i-1/2}}^{x_{i+1/2}} dx \mathbf{S}[\mathbf{U}(x, t)], \quad (15)$$

and $\mathbf{F}_{i\pm 1/2}$ are the fluxes of \mathbf{U} at the grid cell interfaces along the x -direction and are defined as,

$$\mathbf{F}_{i\pm 1/2}(t) = \mathbf{F}(\mathbf{U}(x_{i\pm 1/2}, t)), \quad (16)$$

There are several methods to estimate the physical fluxes at the interfaces by employing various Riemann-solvers. In this work we employ a simple approximation to the Riemann problem *i.e.* the local Lax-Friedrichs flux (LLF), e.g. [37]. The LLF approximation to the point-value flux at the center of a cell interface $x_{i+1/2}$ is given by,

$$\mathbf{F}_{i+1/2} = \frac{\mathbf{F}(\mathbf{U}_{i+1}^-) + \mathbf{F}(\mathbf{U}_i^+)}{2} - \frac{a_{i+1/2}}{2}(\mathbf{U}_{i+1}^- - \mathbf{U}_i^+), \quad (17)$$

where the quantities \mathbf{U}_i^+ , \mathbf{U}_{i+1}^- are fourth-order accurate point values of the conserved quantities at the grid cell interface $x_{i+1/2}$. They are computed from the CWENO4 polynomial $\mathbf{R}_i^1(x)$, $\mathbf{R}^{i+1}_{i+1}(x)$ (discussed below in the subsection III A), respectively and $\mathbf{F}(\mathbf{U}_i^+)$, $\mathbf{F}(\mathbf{U}_{i+1}^-)$ are the respective point value fluxes. The quantity a is the local maximum speed of propagation which is estimated as (see for example, [38]),

$$a_{i+1/2}^x = \max \left\{ \rho \left(\frac{\partial \mathbf{F}^x(\mathbf{U}_i^+)}{\partial U} \right), \rho \left(\frac{\partial \mathbf{F}^x(\mathbf{U}_{i+1}^-)}{\partial U} \right) \right\}, \quad (18)$$

where $\rho(A)$ is the maximum of the magnitude of the eigenvalues of the Jacobian matrix A .

A. Reconstruction of the CWENO4 polynomial from the averages

We construct here a 1D fourth-order CWENO polynomial from the given averages. Before going into the details of the procedure, we note here that the method for reconstructing such polynomials is well described in [33]. Nonetheless, we provide here a summary of the method for the sake of easy implementation.

In this approach we reconstruct a quadratic polynomial $\mathbf{R}_i^1(x)$ in each cell $[i]$, which is a convex combination of three quadratic polynomials $\mathbf{P}^{i-1}_i(x)$, $\mathbf{P}^i_i(x)$ and $\mathbf{P}^{i+1}_i(x)$ such that,

$$\mathbf{R}_i^1(x) = \sum_{l=i-1}^{i+1} w_l^i \mathbf{P}_l^1(x), \quad (19)$$

where the superscript ' i ' appears to distinguish the reconstruction polynomials \mathbf{R} in different grid-cells. The quantities w_l^i are the nonlinear weights which ensure higher-order accuracy in the smooth regions and non-oscillatory behavior near a discontinuity. These weights satisfy the following criteria,

$$\sum_{l=i-1}^{i+1} w_l^i = 1, \quad w_l^i \geq 0, \quad \forall l \in (i-1, i, i+1), \quad (20)$$

and are defined as,

$$w_l^i = \frac{\alpha_l^i}{\alpha_{i-1}^i + \alpha_i^i + \alpha_{i+1}^i}, \quad (21)$$

with,

$$\alpha_l^i = \frac{c_l}{(\epsilon + IS_l^i)^p}, \quad \forall l \in (i-1, i, i+1). \quad (22)$$

Here ϵ , p are chosen to be 10^{-6} and 2, respectively and the constants $c_{i-1} = c_{i+1} = 1/6$, $c_i = 2/3$ are chosen so as to guarantee the fourth order accuracy of the physical quantities at the cell-boundaries [33]. The quantity IS_l^i is the smoothness indicator quantifying the smoothness of the corresponding polynomial $\mathbf{P}_l^1(x)$. It is defined as,

$$IS_l^i = \sum_{n=1}^2 \int_{x_{i-1/2}}^{x_{i+1/2}} (\Delta x)^{2n-1} (\mathbf{P}_l^{i(n)}(x))^2 dx,$$

where $l \in (i-1, i, i+1)$ and n represents the order of the derivative w.r.t. x . All the three coefficients of the quadratic polynomial $\mathbf{P}_l^1(x)$ are obtained uniquely by imposing the conservation of the three averages, $\bar{\mathbf{U}}_{l-1}$, $\bar{\mathbf{U}}_l$ and $\bar{\mathbf{U}}_{l+1}$, where $l \in (i-1, i, i+1)$. Thus, each polynomial, $\mathbf{P}_l^1(x)$, can be written as,

$$\begin{aligned} \mathbf{P}_l^1(x) &= \bar{\mathbf{U}}_l - \frac{1}{24}(\bar{\mathbf{U}}_{l+1} - 2\bar{\mathbf{U}}_l + \bar{\mathbf{U}}_{l-1}) \\ &\quad + \frac{\bar{\mathbf{U}}_{l+1} - \bar{\mathbf{U}}_{l-1}}{2\Delta x}(x - x_l) \\ &\quad + \frac{(\bar{\mathbf{U}}_{l+1} - 2\bar{\mathbf{U}}_l + \bar{\mathbf{U}}_{l-1})}{2\Delta x^2}(x - x_l)^2, \end{aligned} \quad (23)$$

where $l \in (i-1, i, i+1)$. After we reconstruct all the polynomials (\mathbf{P}_{i-1}^i , \mathbf{P}_i^i , \mathbf{P}_{i+1}^i), smoothness indicators can easily be computed using Eq.(23). Nevertheless, we provide here the final expressions of the same for an easy reference.

$$\begin{aligned} IS_{i-1}^i &= \frac{13}{12}(\bar{\mathbf{U}}_{i-2} - 2\bar{\mathbf{U}}_{i-1} + \bar{\mathbf{U}}_i)^2 \\ &\quad + \frac{1}{4}(\bar{\mathbf{U}}_{i-2} - 4\bar{\mathbf{U}}_{i-1} + 3\bar{\mathbf{U}}_i)^2, \end{aligned} \quad (24)$$

$$\begin{aligned} IS_i^i &= \frac{13}{12}(\bar{\mathbf{U}}_{i-1} - 2\bar{\mathbf{U}}_i + \bar{\mathbf{U}}_{i+1})^2 \\ &\quad + \frac{1}{4}(\bar{\mathbf{U}}_{i-1} - \bar{\mathbf{U}}_{i+1})^2, \end{aligned} \quad (25)$$

$$\begin{aligned} IS_{i+1}^i &= \frac{13}{12}(\bar{\mathbf{U}}_i - 2\bar{\mathbf{U}}_{i+1} + \bar{\mathbf{U}}_{i+2})^2 \\ &\quad + \frac{1}{4}(3\bar{\mathbf{U}}_i - 4\bar{\mathbf{U}}_{i+1} + \bar{\mathbf{U}}_{i+2})^2, \end{aligned} \quad (26)$$

Employing the values of the smoothness indicators in Eqs. (21)-(22), nonlinear weights can be computed. These weights are finally used to reconstruct the polynomial $\mathbf{R}_i^1(x)$ in Eq.(19).

Once we know the polynomial $\mathbf{R}_i^1(x)$, we can compute the values of the physical quantities at the grid-cell interface by estimating $\mathbf{R}_i^1(x \pm 1/2) = \mathbf{U}_i^\pm$. For the sake of

convenience, we provide here the formula, all derivation done, for \mathbf{U}_i^\pm from the knowledge of the surrounding cell averages:

$$\begin{aligned} \mathbf{U}_i^+ = & \frac{1}{6} \left[w_{i-1}^i (11\bar{\mathbf{U}}_i - 7\bar{\mathbf{U}}_{i-1} + 2\bar{\mathbf{U}}_{i-2}) \right. \\ & + w_i^i (2\bar{\mathbf{U}}_{i+1} + 5\bar{\mathbf{U}}_i - \bar{\mathbf{U}}_{i-1}) \\ & \left. + w_{i+1}^i (2\bar{\mathbf{U}}_i + 5\bar{\mathbf{U}}_{i+1} - \bar{\mathbf{U}}_{i+2}) \right], \end{aligned} \quad (27)$$

$$\begin{aligned} \mathbf{U}_i^- = & \frac{1}{6} \left[w_{i-1}^i (2\bar{\mathbf{U}}_i + 5\bar{\mathbf{U}}_{i-1} - \bar{\mathbf{U}}_{i-2}) \right. \\ & + w_i^i (2\bar{\mathbf{U}}_{i-1} + 5\bar{\mathbf{U}}_i - \bar{\mathbf{U}}_{i+1}) \\ & \left. + w_{i+1}^i (2\bar{\mathbf{U}}_{i+2} - 7\bar{\mathbf{U}}_{i+1} + 11\bar{\mathbf{U}}_i) \right]. \end{aligned} \quad (28)$$

The values of \mathbf{U}_i^\pm allow us to compute the fluxes $\mathbf{F}_{i+1/2}$ from Eq.(17). In the subsection III B we would discuss how to deal with the source terms.

B. Source terms

We need to be cautious when computing the source terms especially when they are not conservative variables. For example, the viscous term contains a second-order derivative of the velocity v_e (not $n_e v_e$). Note that v_e is not a conservative variable, therefore, in order to maintain the fourth-order accuracy we first have to obtain point values for the density n_e and the momentum density $n_e v_e$. Then we need to divide the point-value of the momentum density by the point-value of the electron density n_e to compute fourth-order accurate point-value of the velocity v_e . For a given averaged quantity $\bar{\mathbf{U}}$, a fourth-order accurate point-value \mathbf{U}_i of at the cell center can be obtained as follows:

$$\mathbf{U}_i = \bar{\mathbf{U}}_i - \frac{1}{24} (\bar{\mathbf{U}}_{i-1} - 2\bar{\mathbf{U}}_i + \bar{\mathbf{U}}_{i+1}) + \mathcal{O}(\Delta x^4). \quad (29)$$

Once we know the point values, a fourth-order approximation to the second-order derivative w.r.t. x can be obtain as below,

$$\begin{aligned} U_{ixx} = & \frac{-U_{i+2} + 16U_{i+1} - 30U_i + 16U_{i-1} - U_{i-2}}{12\Delta x^2} \\ & + \mathcal{O}(\Delta x^4) = W_i(\text{say}), \end{aligned} \quad (30)$$

We then perform a fourth-order accurate averaging procedure to compute corresponding average,

$$\bar{\mathbf{W}}_i = \mathbf{W}_i + \frac{1}{24} (\mathbf{W}_{i-1} - 2\mathbf{W}_i + \mathbf{W}_{i+1}) + \mathcal{O}(\Delta x^4). \quad (31)$$

Note that the operations in Eqs. (29) and (31) are essential only for the source terms which are not conservative variable \mathbf{U} . In case, we fail to do that the overall accuracy of the scheme will be only second-order (see Ref.[37] for a detailed description). In the next section III C, we will discuss the time integration of the semi-discrete scheme (Eq.(13)).

C. Time integration of the semidiscrete scheme

After computing the fluxes $\mathbf{F}_{i\pm 1/2}$ and the source terms $\bar{\mathbf{S}}_i$, Eq.(13) is evolved using a classical fourth order accurate low-storage Runge-Kutta method [39] to achieve the fourth-order accuracy during the temporal evolution. The steps for the same are explained as follows: let us assume that the flux term of Eq.(13) is $\mathbf{C}[\bar{\mathbf{U}}_i]$, now dropping the subscript ‘ i ’ Eq.(13) can be rewritten as,

$$\frac{d\bar{\mathbf{U}}(t)}{dt} = \mathbf{C}[\bar{\mathbf{U}}(t)] + \bar{\mathbf{S}}(t) \quad (32)$$

The intermediate steps to solve Eq.(32) are as follows,

$$\mathbf{K}_1 = \mathbf{C}[\bar{\mathbf{U}}(t_n)] + \mathbf{S}[\bar{\mathbf{U}}(t_n)],$$

$$\bar{\mathbf{U}}_1 = \bar{\mathbf{U}}(t_n) + \frac{\Delta t}{2} \mathbf{K}_1,$$

$$\mathbf{K}_2 = \mathbf{C}[\bar{\mathbf{U}}_1] + \mathbf{S}[\bar{\mathbf{U}}_1],$$

$$\bar{\mathbf{U}}_2 = \bar{\mathbf{U}}(t_n) + \frac{\Delta t}{2} \mathbf{K}_2,$$

$$\mathbf{K}_3 = \mathbf{C}[\bar{\mathbf{U}}_2] + \mathbf{S}[\bar{\mathbf{U}}_2],$$

$$\bar{\mathbf{U}}_3 = \bar{\mathbf{U}}(t_n) + \Delta t \mathbf{K}_3,$$

$$\mathbf{K}_4 = \mathbf{C}[\bar{\mathbf{U}}_3] + \mathbf{S}[\bar{\mathbf{U}}_3],$$

$$\bar{\mathbf{U}}(t_{n+1}) = \bar{\mathbf{U}}(t_n) + \frac{\Delta t}{6} (\mathbf{K}_1 + 2\mathbf{K}_2 + 2\mathbf{K}_3 + \mathbf{K}_4).$$

Here, $n = 0, 1, 2, 3, \dots$ and Δt is determined dynamically according to the Courant-Friedrichs-Lewy (CFL) constraint (see for example, [37]),

$$\Delta t = C_{CFL} \min \left(\frac{\Delta x}{a_{max}} \right), \quad (33)$$

where, C_{CFL} is the CFL number which for all the tests is chosen as, 0.9. The quantities a_{max} is the maximum values of $a_{i+1/2}$, for all ‘ i ’.

In the section IV, we present various numerical tests to validate the implementation of the scheme. We also confirm the fourth-order accuracy of the method for non-linear electron-plasma oscillations.

IV. NUMERICAL TESTS

For all the tests presented in this section we solve Eq.(11) using the periodic boundary conditions and the initial conditions are chosen as follows,

$$n_e(x, 0) = 1 + \delta \cos x, v_e(x, 0) = 0, E(x, 0) = -\delta \sin x. \quad (34)$$

TABLE I: Convergence of error and the EOC for the nonlinear electron plasma oscillations in a cold non-dissipative plasma performed after one period at an amplitude $\delta = 0.35$.

j	1	2	3	4	5	6	7
n_x	128	256	512	1024	2048	4096	8192
L_1 δU	$4.264 \cdot 10^{-4}$	$2.761 \cdot 10^{-5}$	$1.077 \cdot 10^{-6}$	$3.622 \cdot 10^{-8}$	$1.209 \cdot 10^{-9}$	$4.277 \cdot 10^{-11}$	$2.133 \cdot 10^{-12}$
EOC	-	3.94	4.67	4.89	4.90	4.82	4.32

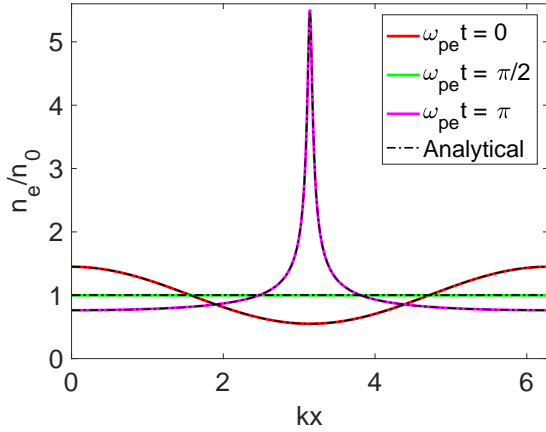


FIG. 1: Comparison between analytical (dashed line points) and numerical profiles (solid lines) of electron density for the nonlinear electron plasma oscillations in a cold non-dissipative plasma at an initial amplitude $\delta = 0.45$

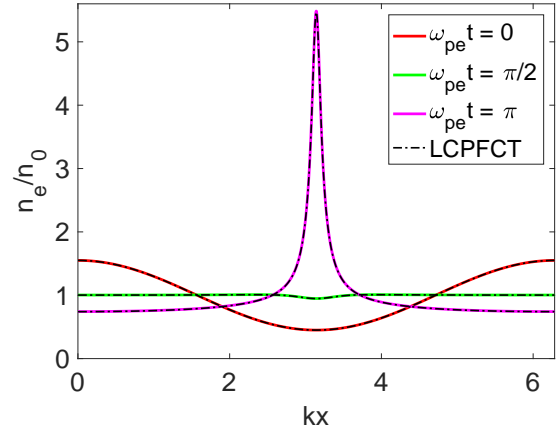


FIG. 3: Comparison between our previous results from the LCPFCT (dashed line points) and from the present numerical scheme (solid lines) where the profiles of electron density for the nonlinear electron plasma oscillations in a cold dissipative plasma at an initial amplitude $\delta = 0.45$ are shown.

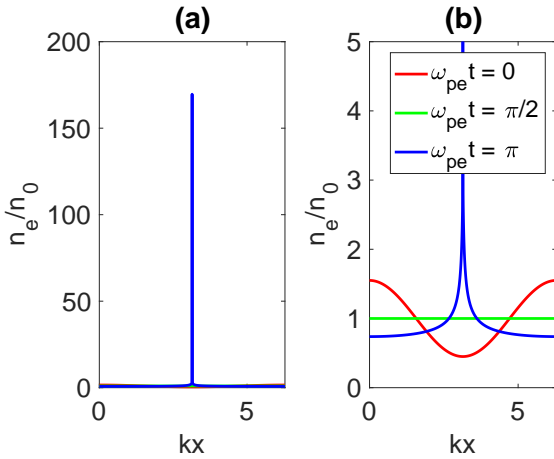


FIG. 2: Space-time evolution of the electron density in the nonlinear electron plasma oscillations in a cold non-dissipative plasma at an initial amplitude $\delta = 0.55$. The left figure (a) shows the density burst, and the right figure (b) is the zoomed version of the left figure which allows one to visualize the density profiles at $\omega_{pe}t = 0$ (in red color) and $\omega_{pe}t = \pi/2$. (in green color). The solid blue lines in both the sub-plots denote the density profile at $\omega_{pe}t = \pi$.

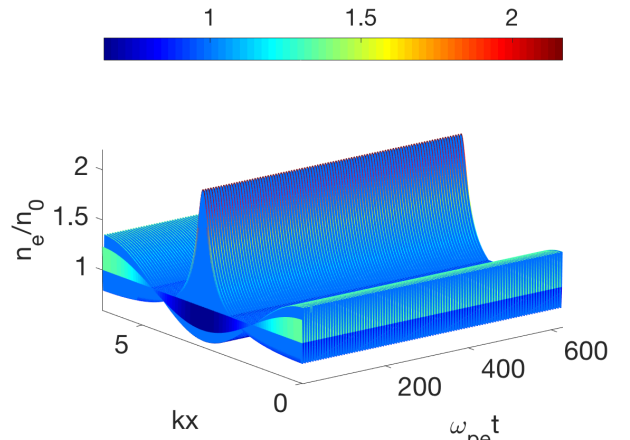


FIG. 4: Space-time evolution of the electron density in a nonlinear electron plasma oscillations in a cold non-dissipative plasma up to $\omega_{pe}t = 200\pi$ at an amplitude $\delta = 0.35$

Number of grid points $n_x = 2048$, which remains the same in all the tests, excluding the convergence study. For the non-dissipative plasma $\nu_0 = \eta = 0$, however, for the dissipative plasma $\nu_0 = 0.03$ and $\eta = 2 \times 10^{-5}$ which are same as the ones chosen in Ref. [2] for one

of the tests. Various values of δ are chosen for different tests. For example, in order to verify the correctness of the numerical scheme, in Fig.1 we first compare the evolution of the nonlinear electron plasma oscillations in a cold non-dissipative with the previously established analytical results [8]. Here we choose $\delta = 0.45$ same as in [8]. The solid lines in the figure denote the results from our simulations, and the dashed line points stand for the analytical results [8]. A good agreement between the theory and the simulation is witnessed in this test.

It is well known [8] and also confirmed in numerical simulations [4, 40] that in a cold non-dissipative plasma the nonlinear electron plasma oscillations, initiated by a sinusoidal density perturbation, break at $\omega_{pe}t = \pi$ when the initial amplitude $\delta \geq 0.5$. In Fig.2 we show the evolution of the same at an initial amplitude $\delta = 0.55$ and observe a density burst (a signature of wave-breaking) $\omega_{pe}t = \pi$. We stop the simulation at the first density burst because the results from the fluid simulations are not physically valid after the wave-breaking.

In our previous work, we have numerically studied the nonlinear electron plasma oscillations in cold dissipative plasma for the constant viscosity $\nu_0 = 0.03$ and resistivity $\eta = 2 \times 10^{-5}$ and found that the oscillations initiated by the sinusoidal density perturbation do not break even when $\delta = 0.55 (> 0.5)$. In Fig.3, we compare the results from the present and previous simulations for the same parameters, where the solid lines in the figure are from the present simulation and the dashed line points represent the old results from the LCPFCT simulation [2]. Both the results exhibit a good agreement between the two.

In order to demonstrate the stability and the negligible numerical dissipation of the present numerical method, we show in Fig.4 the space-time evolution of the electron density profile in a cold non-dissipative plasma up to one hundred electron plasma oscillations at an amplitude $\delta = 0.35$. No unphysical effects such as numerical noise are observed here.

Moreover, we also confirm the fourth-order accuracy of the numerical scheme, as shown in Table.I, by estimating the error for the nonlinear electron plasma oscillations in a cold non-dissipative plasma at different spatial resolutions after one period $\omega_{pe}t = 2\pi$. Here we compute the L_1

norm of the error as follows,

$$\delta U = \frac{1}{n_x} \sum_{i=1}^{n_x} |U_i^f - U_i^0|, \quad (35)$$

where U_i^0, U_i^f are the initial (at $\omega_{pe}t = 0$) and the final (at $\omega_{pe}t = 2\pi$) profiles of the electron density the numerical solutions as a function of grid resolution and n_x is the number of grid points.

After computing the norms of the errors, we obtain the experimental order of convergence (EOC) using the formula,

$$EOC(j+1) = \frac{|\log(L_1(n_x(j+1)))| - |\log(L_1(n_x(j)))|}{|\log(n_x(j+1))| - |\log(n_x(j))|}, \quad (36)$$

here j runs from 1 to 7.

V. SUMMARY AND DISCUSSION

In summary, we have presented here an easy-to-implement higher-order finite volume scheme to study the nonlinear behavior of the non-relativistic electron-plasma oscillations in the cold dissipative and non-dissipative plasmas. The correctness of the new scheme has been established by reproducing previous analytical and numerical results for both non-dissipative and dissipative cold plasmas. The stability and the least dissipative nature of the numerical scheme have been confirmed by following the evolution of the nonlinear electron plasma oscillations up to hundred plasma periods, and the fourth-order accuracy has also been demonstrated by evaluating the error at various grid resolutions after one plasma period. Extension of the present method for the warm and magnetized plasma is straightforward. Implementations of the relativistic effects and multi-component plasma are in progress and would be published elsewhere.

ACKNOWLEDGMENTS

The author would like to thank Dr. Yannick Marandet for valuable suggestions.

-
- [1] N. Jain, A. Das, P. Kaw, and S. Sengupta, *Physics of Plasmas* **10**, 29 (2003).
 - [2] P. S. Verma, J. Soni, S. Sengupta, and P. Kaw, *Physics of Plasmas* **17**, 044503 (2010).
 - [3] P. S. Verma, S. Sengupta, and P. Kaw, *Physical Review Letters* **108**, 125005 (2012).
 - [4] P. S. Verma, S. Sengupta, and P. Kaw, *Physical Review E* **86**, 016410 (2012).
 - [5] P. S. Verma, *Physics Letters A* (2017).
 - [6] P. S. Verma and T. C. Adhyapak, *Physics of Plasmas* **24**, 112112 (2017).
 - [7] J. M. Dawson, *Physical Review* **113**, 383 (1959).
 - [8] R. Davidson and P. Schram, *Nuclear Fusion* **8**, 183 (1968).
 - [9] P. K. Kaw, A. Lin, and J. Dawson, *The Physics of Fluids* **16**, 1967 (1973).
 - [10] L. Stenflo and O. Gradov, *Physical Review E* **58**, 8044 (1998).
 - [11] S. S. Gupta and P. K. Kaw, *Physical Review Letters* **82**, 1867 (1999).
 - [12] G. Rowlands, G. Brodin, and L. Stenflo, *Journal of Plasma Physics* **74**, 569 (2008).

- [13] S. Sengupta, V. Saxena, P. K. Kaw, A. Sen, and A. Das, *Physical Review E* **79**, 026404 (2009).
- [14] C. Maity, N. Chakrabarti, and S. Sengupta, *Physics of Plasmas* **17**, 082306 (2010).
- [15] C. Maity, N. Chakrabarti, and S. Sengupta, *Physical Review E* **86**, 016408 (2012).
- [16] C. Maity, A. Sarkar, P. K. Shukla, and N. Chakrabarti, *Physical Review Letters* **110**, 215002 (2013).
- [17] G. Brodin and L. Stenflo, *Physics Letters A* **378**, 1632 (2014).
- [18] G. Brodin and L. Stenflo, *Physics of Plasmas* **21**, 122301 (2014).
- [19] G. Brodin and L. Stenflo, *Physics Letters A* **381**, 1033 (2017).
- [20] G. Brodin and L. Stenflo, *Physics of Plasmas* **24**, 124505 (2017).
- [21] J. Faure, Y. Glinec, A. Pukhov, S. Kiselev, S. Gordienko, E. Lefebvre, J.-P. Rousseau, F. Burgy, and V. Malka, *Nature* **431**, 541 (2004).
- [22] N. Jain, T. Antonsen Jr, and J. Palastro, *Physical Review Letters* **115**, 195001 (2015).
- [23] C. K. Birdsall and A. B. Langdon, *Plasma physics via computer simulation* (CRC Press, 2004).
- [24] D. Mandal and D. Sharma, in *Journal of Physics: Conference Series*, Vol. 759 (IOP Publishing, 2016) p. 012068.
- [25] H. Schamel, D. Mandal, and D. Sharma, *Physics of Plasmas* **24**, 032109 (2017).
- [26] R. K. Bera, S. Sengupta, and A. Das, *Physics of Plasmas* **22**, 073109 (2015).
- [27] R. K. Bera, A. Mukherjee, S. Sengupta, and A. Das, *Physics of Plasmas* **23**, 083113 (2016).
- [28] J. P. Boris and D. L. Book, *Journal of computational physics* **135**, 172 (1997).
- [29] D. Levy, G. Puppo, and G. Russo, *Applied Numerical Mathematics* **33**, 407 (2000).
- [30] C.-W. Shu, *SIAM Review* **51**, 82 (2009).
- [31] D. Levy, *Systém hyperboliques: Nouveaux schémas et nouvelles applications* **1**, 489.
- [32] F. Bianco, G. Puppo, and G. Russo, *SIAM Journal on Scientific Computing* **21**, 294 (1999).
- [33] D. Levy, G. Puppo, and G. Russo, *ESAIM: Mathematical Modelling and Numerical Analysis* **33**, 547 (1999).
- [34] D. Levy, G. Puppo, and G. Russo, *SIAM Journal on scientific computing* **24**, 480 (2002).
- [35] D. Levy, G. Puppo, and G. Russo, *Applied Numerical Mathematics* **33**, 415 (2000).
- [36] D. Levy, G. Puppo, and G. Russo, *SIAM Journal on Scientific Computing* **22**, 656 (2000).
- [37] P. S. Verma and W.-C. Müller, *Journal of Scientific Computing* , 1 (2017).
- [38] A. Kurganov and D. Levy, *SIAM Journal on Scientific Computing* **22**, 1461 (2000).
- [39] J. Williamson, *Journal of Computational Physics* **35**, 48 (1980).
- [40] P. S. Verma, S. Sengupta, and P. K. Kaw, *Physics of Plasmas* **18**, 012301 (2011).